3D modelling of rifting through a pre-existing stack of nappes in the Gulf of Corinth (Greece): a mixed analogue/numerical approach

L. LE POURHIET[1,2*], L. MATTIONI[2**] & I. MORETTI[2]

[1]*Laboratoire de Tectonique, Université Pierre et Marie Curie, Paris, France (e-mail: laetitia@gps.caltech.edu)*

[2]*Institut Français du Pétrole, Rueil Malmaison, France*

**Now at Caltech, Pasadena, CA, USA*

***Now at Beicip Franlab, Rueil Malmaison, France*

Abstract: The Gulf of Corinth is a young (1 Ma) active rift currently extending N00, which displays significant contrasts in structural style along strike. A possible explanation for these variations is the presence of the Phyllades nappe in the basement of the western part of the Gulf. Previous 2D thermo-mechanical models have shown that a strong strength contrast between this metamorphic unit and the rest of the basement can explain the kinematics and the spacing of the faults in the western part. The rift, however, displays a wide variety of 3D features (e.g., en echelon faulting, N30 transverse normal faults) that cannot be taken into account using 2D modelling. To obtain 3D insights into the role of an inherited dipping weakness zone, analogue (sand and PDMS) experiments based on the results of the 2D numerical thermo-mechanical model have been performed. The analogue models show that a 30° discrepancy between the dipping direction of the weak nappe and the direction of extension leads to the formation of en echelon and N30 striking normal faults as observed in the Gulf of Corinth. However, fault spacing and graben width completely misfit both the data and the results of the thermo-mechanical models on which the analogue experiments were based. In order to understand those differences, numerical mechanical benchmarks of the analogue experiments have been run to test different factors (3D lateral displacements, values of the elastic parameters and bottom boundary conditions) that could have affected the dynamics of the analogue model. This approach highlights, for our case study, that the misfits are mostly related to the lack of isostatic compensation at the base of the analogue experiments.

Geological setting

The area of the Gulf of Corinth has been in a continuous extensional regime since the middle Miocene (Jolivet *et al.* 1994; Jolivet & Faccenna 1999). This contribution deals with the last rifting event that has taken place for the last 1 to 1.5 Ma in the area, but as the long-term extension affects the structures, both the long-term and the neotectonic features will be briefly discussed in the following.

In the external zone of the Hellenides, long-term extension has led to the exhumation of metamorphic core complexes along ductile shear zones. In the Peloponnesus, the shear strain associated with these detachments is mainly localized inside the Phyllades nappe (Fig. 1). One of the core complexes crops out at the southern limit of the Gulf of Corinth in the Zarouchla tectonic window (outlined by strips in Fig. 1). The average strike of the stretching lineations affecting this dome structure is parallel to the Miocene direction of extension (i.e., N30 to N50). Hence, at the onset of the neotectonic rifting event, the Phyllades nappe was already retromorphosed from the lowest pressure in the blue schist metamorphic facies to the epimetamorphic facies.

The present day geometry of the shoreline of the Gulf of Corinth shows that the mean topography decreases eastwards. Moho depth follows the same trend (Makris 1978; Tiberi *et al.* 2001). This positive correlation, at the scale of the Gulf, suggests that the base of the crust is isostatically compensated and that the large-scale topographic gradient remains from long-term extension. The widening of the Gulf to the east is also compatible with a clockwise rotation of the Peloponnesus, as inferred from paleomagnetic data (e.g., Duermeijer *et al.* 2000), and reflects the fact that the finite extension has

From: BUITER, S. J. H. & SCHREURS, G. (eds) 2006. *Analogue and Numerical Modelling of Crustal-Scale Processes.* Geological Society, London, Special Publications, **253**, 233–252.
0305-8719/06/$15.00

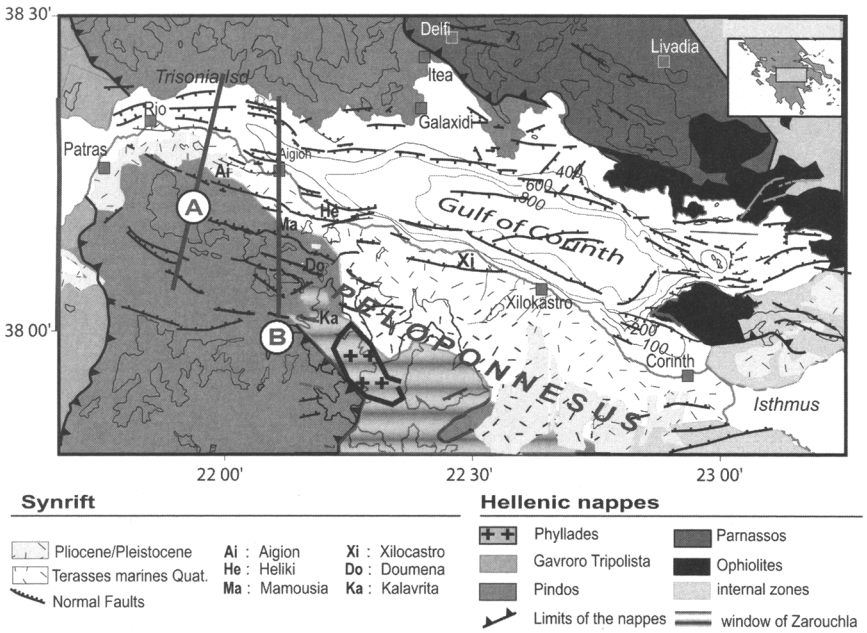

Fig. 1. Structural map of the Gulf of Corinth. Faults after Moretti (2004), limits of the nappes after Aubouin *et al.* (1970). A and B lines correspond, respectively, to the location of the geological cross-section (Moretti 2004) displayed in Fig. 5 and to the micro-seismic cross-section of Rigo (1996) used to constrain the validity of the thermo-mechanical models.

been much greater in the central Aegean domain than in the external part of the Hellenides.

At the onset of rifting, the eastern part of the rift was indeed connected to the Aegean Sea at the level of the Corinth Isthmus and Megara basin further east (Bentham *et al.* 1991). Because the western part of the current rift was still under compression until the Pliocene (Doutsos & Kokkalas 2001), the basin was closed by the Hellenides belt at the level of Patras and, therefore, has not been affected by long-term extension. The sediments from this side of the rift as well as the oldest dated calcite steps found along fault planes are early Pleistocene in age (i.e., <1 Ma; see Causse *et al.* 2004). This timing is compatible with the onset of dextral displacement on the Kefalonia fault (Cocard *et al.* 1999); a strike slip fault located further west. These data suggest a change in the regional kinematics by 1.5 Ma that could explain the discrepancies between geological observations and GPS measurements (Briole *et al.* 1999). GPS data indicates that the current direction of extension is N00 and that the rate of extension increases westward from 0.5 cm/yr at the level of the Corinth Isthmus to 1.5 cm/yr at the level of Patras. This anticlockwise rotation of the Peloponnesus with respect to the northern margin of the Gulf is not compatible with the paleomagnetic data. Therefore, given the short (60 km) length-scale of the Gulf of Corinth, the current rifting phase can be treated separately from the Neogene long-term extension.

From a structural point of view, the Quaternary rift is usually described as an asymmetric graben because the southern shore is covered by uplifted deposits of marine fan deltas and continental Guilbert's fan deltas (Ghisetti *et al.* 2001; Malartre *et al.* 2004), whereas, on the northern shore, the pre-rift basement crops out directly. Although some beach-rocks are locally uplifted, the northern shore is stable or slightly subsiding in general (Lykousis *et al.* 1998).

The Gulf of Corinth is segmented along strike (Ghisetti & Vezzani 2004). In the central-eastern part of the rift, the syn-rift deposits are located in one main graben in which faulting is roughly symmetrical (Stefatos *et al.* 2002). However, the marine terraces uplifted on the southern shore indicate a subsisting asymmetry of the shore (Armijo *et al.* 1996). At the eastern tip, the Gulf is divided into two grabens bordered by faults dipping 45° and branching at the base

of the seismogenic zone, which is located much deeper (i.e., 15 to 20 km) than in the west (Jackson *et al.* 1982). These faults have two main strike directions: N90° and N30°. The first ones were responsible for the 1981 earthquake. The last ones were responsible for the closure of the connection between the Gulf and the Aegean Sea during the Quaternary.

In the western part, the basin is elongated N120. The southern shore line reflects the en echelon disposition of the major faults. Their strikes are perpendicular to the current direction of extension (i.e., N90° to N110°, see Moretti *et al.* 2003). N30° normal faults are highlighted by microseismic events (Lyon Caen *et al.* 2004), micro-gravimetric survey (Mrlina 2004*a*, *b*) and seismic reflection data (Naville *et al.* 2004). These normal faults act as transfer between the N90 faults.

On the southern shore, sedimentation has been controlled by numerous and closely spaced faults forming a series of small isolated half grabens. The age of those grabens seems to decrease northward (Flotté 2002; Micarelli *et al.* 2003). Flotté (2002) used anticline deformation data of the syn-rift deposits to constrain kinematic reconstructions of the fault décollement level based on a roll-over model. His models imply that such a level deepens northwards. However, he was not able to propose a conceptual model explaining mechanically that fault spacing reduces from 8 km to 4–2 km in the direction of deepening of the inferred décollement level.

The microseismic and seismic events recorded in the western Gulf of Corinth also outline a northward dipping zone. Moreover, reconstruction of focal mechanisms of the earthquakes located inside this zone indicate very low angle nodal planes (i.e., 10°–30°, Rigo *et al.* 1996; Rietbrock *et al.* 1996) and thus favour the possibility for seismicity along shallow dipping fault(s). Seismologists tend now to agree on the fact that the outcropping major faults are planar up to the base of the seismogenic zone. Although the relation between the low-angle seismic events and the high-angle faults is not yet well understood, the low-angle dipping zone is clearly associated with the presence of fluids, as shown by anomalies in the Vp × Vs (velocity of P-wave × velocity of S-wave) tomography (Latorre *et al.* 2004) and in the magneto-telluric conductivity (Pham *et al.* 2000).

Modelling approach

Based on the observations that (1) the spacing of the normal faults decreases in the same direction as the postulated décollement level deepens and that (2) the N120/N30 direction appears everywhere along this structure, Le Pourhiet *et al.* (2004) proposed that the N120° overall direction of the western part of the Gulf is inherited from the Neogene syn-orogenic extension. Their fully coupled 2D thermo-mechanical models include a weak dipping layer in the pre-rift basement, because:

(1) The southern fault of the zone affected by Quaternary rifting is observed to root at low angle on the Phyllades nappe, in the field (Flotté, 2002).
(2) The Phyllades tectonic unit was originally a pelitic deep basin deposit and was exhumed during the late Miocene (L. Jolivet, pers. comm. for the Gulf of Corinth; Trotet 2000 in the South Peloponesus). During its burial and exhumation, it has been enriched in anisotropic phyllosilicates known to be very weak in the ductile (Ranalli 1987) as in the plastic regime (Bos & Spiers 2002).
(3) Tiberi *et al.* (2001) evidence by means of gravity measurements, a very strong anomaly elongated N120, located at the place where the Phyllades crop out.

Once the presence of the weak dipping nappe in the basement of the Gulf of Corinth is established, thermo-mechanical models have been used to quantify the dynamic influences of the presence of a weak dipping nappe. The weakness of the heterogeneity has been set as a parameter and models have been computed for a wide range of competences. After comparing the kinematics and stress distribution in the model to the fault spacing, earthquakes distribution and fault kinematics in the Gulf of Corinth, it has been found that only a very weak nappe can explain the rotation of P and T axes for the relatively deep earthquakes, the shallow décollement level (inferred from rollover), and the fault spacing in the western part of the Gulf of Corinth.

As a step forward in the understanding of the Gulf of Corinth, this paper and Mattioni *et al.* (2006) aim to verify that the non co-linearity between the current direction of extension and the dipping direction of the weak nappe leads to the formation of en echelon structures similar to those observed in the Gulf of Corinth. 3D analogue models have been designed using the effective rheology (elasto-plastic v. viscous) obtained from the numerical thermo-mechanical computations. Despite this effort made in fitting the effective rheologies, major discrepancies exist in the shape of the graben (width, fault spacing).

Possible causes of these discrepancies fall into three categories: (1) The plane strain assumption in the thermo-mechanical model. (2) The rheological assumptions in the analogue models, e.g., neglecting the elastic effect in the overall model, neglecting plasticity in the weak layer. (3) The basal boundary conditions in the analogue models.

In order to explore the potential impact of these factors, numerical benchmarks of the analogue experiments have been carried out. This part of the study shows how a coupled approach using both 2D numerical modelling and 3D analogue modelling gives better insights into the validity of the models and their relevance for solving geodynamic issues.

After a description of the two modelling tools, the set-up and results of Le Pourhiet *et al.* (2004) are briefly described, as well as a similar thermo-mechanical experiment that will be used as reference for the present study. We then focus on the set-up of the analogue experiments and their results. After comparing the new coupled thermo-mechanical model with the analogue experiments, the paper will seek an explanation for the large discrepancies observed between both approaches, by computing numerical benchmarks of the analogue models and varying the different parameters listed above.

Modelling techniques

Numerical approach

We use Paravoz, a fast Lagrangian analysis of continua (FLAC)-based thermo-mechanical code (Cundall 1989; Poliakov *et al.* 1993). This code solves Newton's second law

$$\rho g_i + \frac{\partial \sigma_{ij}}{\partial x_j} = \rho \frac{\partial V_i}{\partial t} \tag{1}$$

and Fourier's law for heat transfer

$$\frac{DT}{Dt} = \frac{\partial}{\partial x_i}\left(\chi \frac{\partial T}{\partial x_i}\right) + \frac{H_r}{\rho C_p} \tag{2}$$

where ρ = mean density, g = gravity acceleration, σ = stress tensor, x = spatial coordinates, V = velocity, t = time, χ = thermal diffusivity, T = temperature, H_r = radiogenic heat production, C_p = heat capacity. Einstein summation applies for repeated indices.

These partial differential equations are solved using a fully coupled (including thermal stress/shear heating) explicit scheme on a Lagrangian mesh using a mixed (element/nodes) discretization to avoid mesh locking (Cundall & Board 1988). Large strain computations are allowed by remeshing as soon as one of the corners of the triangular mesh reaches a critical minimum angle of 10°. As the remeshing process includes linear interpolation of nodal values (velocity, temperature) and closest neighbour redistribution of elementary values (stresses, physical properties including finite strain), it should be avoided as much as possible for the sake of precision.

Heat advection is implicitly solved considering the rate of deformation of the mesh as indicated by the objective time derivative D in Fourier's equation. The explicit time-marching aspect of this numerical method implies very small time steps and thus enables various non-linear visco-elasto-plastic rheologies to be handled easily. In shear, each element behaves either as compressible an elasto-plastic or Maxwell visco-elastic body, depending on which of these two rheologies produces the lowest value of the second invariant of stress tensor.

Maxwell body behaviour can be written following an incremental rule:

$$\begin{cases} \sigma_{ij} = \sigma_{ij}^{\text{old}} + \dfrac{\partial \tau_{ij}}{\partial t}\Delta t + \delta_{ij}\dfrac{\partial \bar{\sigma}}{\partial t}\Delta t \\ \dfrac{\partial \tau_{ij}}{\partial t} = 2G\left(e_{ij} - \dfrac{\tau_{ij}}{2\mu_{\text{shear}}(T, e^{\text{II}})}\right) \\ \dfrac{\partial \bar{\sigma}}{\partial t} = K\nabla \cdot \mathbf{V} \end{cases} \tag{3}$$

where δ is the Kronecker delta, G and K are respectively the shear and bulk modulus, and e^{II} is the second invariant of the strain rate tensor e, while τ is the deviatoric part of the stress tensor, and $\bar{\sigma}$ is its trace divided by 3. μ_{shear} is the effective dynamic viscosity. It can be set as a constant or may depend on the second invariant of deviatoric strain-rate tensor following the 3D formulation of the power law creep flow rules described in Chen & Morgan 1990.

$$\mu_{\text{shear}}(T, e^{\text{II}}) = \frac{1}{4}(e^{\text{II}})^{((1/n)-1)}\left(\frac{3}{4}A\right)^{-1/n} \times \exp\left(\frac{E}{n\text{RT}}\right) \tag{4}$$

Here, E, A and n are the common non-Newtonian creep parameters obtained from uni-axial creep experiments; T and R are the absolute temperature and the gas constant respectively.

As the time steps are small, a simple elastic predictor/plastic corrector technique is used to

compute the non-associated Mohr–Coulomb elasto-plastic flow. This means that when the predicted elastic state of stress reaches the yield criterion f^s, which depends on the internal friction angle Φ of the material,

$$N_\Phi = \frac{1+\sin\Phi}{1-\sin\Phi}$$
$$f^s = \sigma 1 - \sigma 3 N_\Phi + 2C_0\sqrt{N_\Phi} \qquad (5)$$
$$f^s \leq 0 \Rightarrow \text{rupture}$$

The plastic strain $\varepsilon^{\text{plas}}$ is assumed to be proportional by a scalar factor λs to the derivative versus stress of plastic potential Qs. Qs depends on the dilatancy angle $\Psi \ll \Phi$ for rocks.

$$N_\Psi = \frac{1+\sin\Psi}{1-\sin\Psi}$$
$$Qs = \sigma 1 - \sigma 3 N_\Psi \qquad (6)$$
$$\varepsilon^{\text{plas}} = \lambda s \frac{\partial Qs}{\partial \sigma}$$

The plastic multiplier λs is found assuming that in a static yield regime, stresses stay on the yielding surface for consistency (Eqn. 7) reasons (for details see Vermeer & Deborst 1984).

$$\dot{f}^s = 0 \qquad (7)$$

An explanation of the boundary conditions that are used in the numerical models is given in Figure 2.

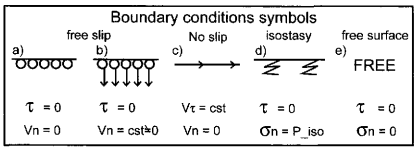

Fig. 2. Type of mechanical boundary conditions: (**a**) and (**b**) Free slip means that the orthogonal velocity is set to a constant (Vn) and the tangential stress (τ) to zero. (**c**) No slip means that the tangential velocity is set to a constant ($V\tau$) and normal velocity (Vn) is set to zero. (**d**) Local isostasy means that shear stress (τ) is set to zero and normal stress is (σn) calculated with reference to a hypothetic isostatic compensation level at depth. (**e**) Free means that both normal (σn) and shear stress (τ) components are set to zero on the boundary. It constitutes a realistic boundary condition to model the Earth's surface and topography for Lagrangian mesh.

Analogue approach

The analogue experiments are described in further detail in Mattioni *et al.* (2006) and are only briefly described here.

The experiments are analysed by x-ray tomography (Colletta *et al.* 1991), a non-destructive technique that allows the 4D acquisition of the analogue model density (and thus material) distribution.

In the experiments, upper-crustal brittle rocks are simulated with sand and glass powder (Pyrex, usually used together with sand to get a better visualization of the results with the x-ray scanner). Their internal friction angles are 34° and 42°, respectively, while their densities range from 1500 to 1700 kg/m^3, depending on their compaction (note that the sand pile was not pre-compacted in the experiments). As dry granular media are dilatant in shear, the shear bands are easy to image by x-ray tomography as they represent narrow zones of reduced density.

In the present experiments, the Pyrex layer is 3 mm thick and is located 3 mm below the surface at the initial stage, approximately in the middle of the elasto-plastic layer that does not contain the weak dipping heterogeneity.

The ductile behaviour of rocks in the lower crust, and/or of weak layers within the brittle upper crust, is simulated by silicone putty (PDMS) presenting a much lower density than sand (965 kg/m^3) and therefore appearing darker on the cross-sections. PDMS behaves as a nearly Newtonian fluid with a viscosity of 2×10^4 Pa at room temperatures and at strain-rates below 3×10^{-3} s^{-1} (Weijermars 1986).

In order to be considered analogue to Earth, physical experiments have to be properly scaled. This means that the dimensionless physical properties that govern the modelled process must be equal in the analogue experiment and in nature (Ramberg 1981). In this study, the scaling of the physical experiments has followed classical rules for sand silicone experiments, thus neglecting the main governing factor for fault spacing, i.e., elasticity. However, the adjective 'analogue' is used instead of 'physical' to describe the experiments throughout our paper for consistency with other papers in this volume.

In the analogue experiments, extension is applied using diverging plastic sheets which are fixed to smooth diverging walls. Friction along those walls is taken to be negligible compared to the friction in the granular media. In the direction orthogonal to extension, the experiments are bordered by two rubber sheets which are used to simulate free slip boundaries.

Comparing numerical and analogue results

Two main outputs have been chosen: topography and cumulative plastic strain. Although topography stands as a straightforward control parameter, one should note that (1) in the numerical scheme of Paravoz a slight diffusion is applied at the top of the models to reduce the occurrence of remeshing, and (2) as the Pyrex (which has a higher angle of internal friction) is not assigned any geological meaning, it has not been taken into account in the numerical model and will be considered as a possible factor introducing modelling artefact in the analogue approach. The numerical topographies are therefore always slightly smoother than those obtained by analogue modelling.

The second control parameter is cumulative plastic strain. It has been chosen because the dark strips, interpreted as faults in the analogue models, correspond in fact to a dilatation zone associated with plastic shear. For underconsolidated sand (as the case in the present analogue experiments), the dilation is theoretically supposed to be proportional to the plastic shear strain after 2% shear strain (Vermeer 1990). Before this critical strain, the shear bands compact slightly and thus will either not be visible by x-ray tomography or appear with lighter tones. It is thus predictable that some shear bands with low amounts of shear strain or diffuse plastic strain zones predicted by numerical modelling will not be visible through x-ray acquisition in the analogue models.

From 2D thermo-mechanical to 3D analogue models

Thermo-mechanical experiments

All thermo-mechanical experiments were run with Paravoz using a visco-elasto-plastic flow rule including non-Newtonian temperature-dependent viscosity and full thermal coupling. The space was discretized in quadrilateral elements which are initially 200 × 200 m. The mechanical parameters of the runs displayed in this paper are listed in Table 1. The thermal parameters C_p and χ have been set constant for all materials (i.e., 1000 J kg^{-1} K^{-1} and 3 W m^{-1} K^{-1} respectively) as well as H_r, which decreases exponentially with depth according to characteristic decay of $1/e$ for 12 km, taking $H_0 = 10^{-9}$ W kg^{-1} at the surface for all the materials.

Le Pourhiet *et al.* (2004) aimed at getting a better understanding of the impact of a pre-existing weak dipping nappe on the kinematics of faulting during the early stages of rifting. The weak nappe was introduced in the model as a shallow dipping layer (20°) possessing different mechanical properties. The thickness of the nappe (1.5 km), the size of the experiments (60 × 15 km) and the boundary condition were kept constant in the study (Fig. 3a), while two parameters were raised: (1) the contrast in Maxwell relaxation time between the weak dipping nappe and the rest of the pre-rift basement, (2) the pre-rift basement relaxation time. The contrast was obtained by keeping the elastic properties constant as well as the activation energy E and the coefficient n in the creep power law, and by varying the pre-exponential parameter A for the different lithologies. These experiments show that the presence of a weak dipping nappe in the upper crust leads to a local reduction of the integrated strength of the upper crust (Fig. 3b). Consequently, strain localization occurs at a very specific location, the brittle-ductile transition (BDT) of the weak dipping heterogeneity. The parametric study has led to the conclusion that a very weak nappe was indeed needed to avoid the localization on one main decollement level (Fig. 3c) and hence to reproduce the fault spacing, the kinematics and the micro-seismicity depth distribution of the western part of the Gulf of Corinth.

However, to reduce the boundary effects in the analogue models, it was not possible to set the initial geometry of the analogue experiments to the same initial width as in Le Pourhiet *et al.* (2004). Therefore, a new thermo-mechanical run was performed using 102 km instead

Table 1. *Mechanical parameters of the thermo-mechanical experiment*

Material	Density, ρ (kg m^{-3})	$A^{\ddagger}$ (MPa^{-n})	$n^{\ddagger}$	$E^{\ddagger}$ (J mol^{-1})	Young's modulus, E (Pa)	Cohesion (Pa), C_0	Friction angle, Φ (°)
WN*	2600	5×10^{3}	3	1.9×10^{5}	7.5×10^{10}	2×10^{7}	30°
SB†	2600	5×10^{-6}	3	1.9×10^{5}	7.5×10^{10}	2×10^{7}	30°

*WN: weak nappe.
†SB: strong basement.
‡Coefficients for non Newtonian creep law are taken from Le Pourhiet *et al.* (2004).

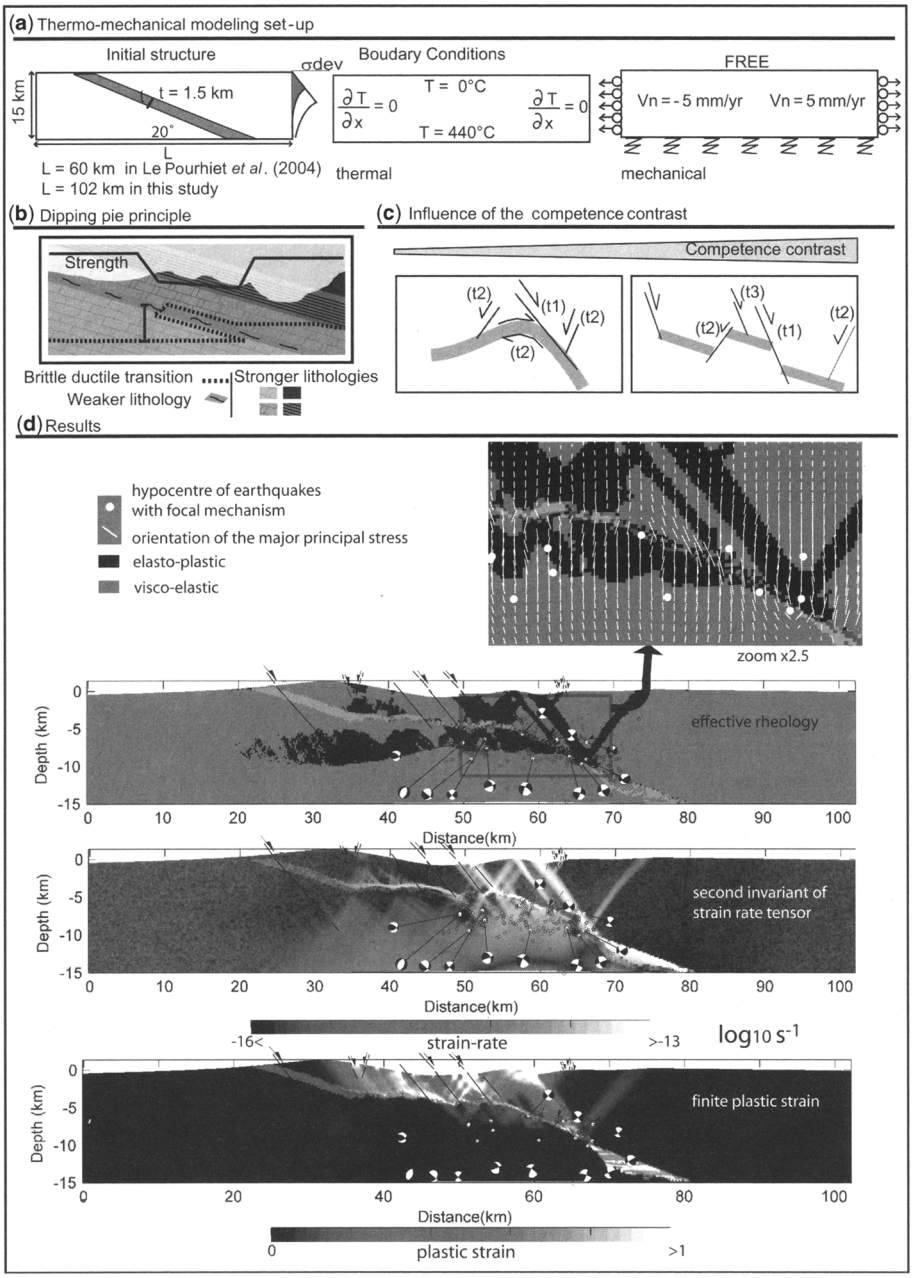

Fig. 3. (**a**) Initial geometry of the thermo-mechanical models; a unique weak nappe is represented in grey. Schematic yield strength envelope for the weak heterogeneity and the strong surrounding are drawn on the right. t is the thickness of the weak nappe. The brittle ductile transition of the weak nappe and background white material are the parameters of the study. The last two boxes display the boundary conditions of the thermo-mechanical models for the thermal and the mechanical parts, respectively. (**b**) The dipping pie conceptualizes a layered media on which stress is not applied parallel to the layers but with a slight angle. It applies to any stack of inhomogeneous units and implies local reduction of the strength (thick black line) of the upper crust associated with lateral variations of the depth of the brittle ductile transition (BDT = dashed line). (**c**) Resulting fault kinematics and distribution as a function of competence contrast. Numbers in brackets indicate the relative timing of faulting. (**d**) Comparison between the results of a thermo-mechanical run and the fault pattern and micro-seismic data from the Gulf of Corinth (Rigo *et al.* 1996).

of 60 km as initial width in the stretching direction, the rest of the parameters remaining unchanged.

The results of the new experiment are shown in Figure 3d. Although the strain rate is now slightly lower, the results obtained with this wider version are similar to those obtained in the previous study in terms of fault spacing and kinematics of faulting, i.e., some of the faults cross the weak nappe and root at the BDT of the upper crust, while the first fault and some out-of-sequence faults root at lower depth on the weak heterogeneity. After 1.5 Ma of extension, there is a good agreement with the fault spacing (i.e., finite plastic strain), the distribution of active faults, the depth distribution of the micro-seismicity, as well as the orientation of the principal stress direction at depth as inferred in the western part of the present day Gulf of Corinth.

Analogue experiments

Set-up. The dimension of the sandbox is determined by the size of the medical scanner (i.e., 0.7×0.255 m). In order to be able to compare numerical and analogue models, the material distribution (i.e., granular or PDMS) in the analogue experiments should reflect the effective rheology (i.e., elasto-plastic or viscous) of the thermo-mechanical experiments. *Sandbox* experiments, unlike numerical experiments, do not enable the temperature dependence of the viscosity to be taken into account. Therefore, an arbitrary limit between the effectively brittle and effectively viscous domain has to be introduced. In order to set this limit, a comparison between the Maxwell relaxation time and the characteristic timescale of our control parameter (i.e., the fault formation and migration relevant for the Gulf of Corinth) has been made. We arbitrarily decided that the part of the thermo-mechanical models having a Maxwell characteristic time five times lower than the time needed to create a new fault, are considered to behave viscously while the rest is considered to behave as an elasto-plastic body. As the faulting timescale is 100 ka, the limit we are seeking corresponds to a Maxwell characteristic time of 20 ka. Taking into account the shear modulus $G = 3 \times 10^{10}$ Pa, this limit corresponds to an effective viscosity of 10^{22} Pa in the thermo-mechanical models.

Because the aim of the study is to get insight into the 3D structure of the Gulf of Corinth, the initial material distribution of the analogue models (Mattioni *et al.* 2006) has been determined using the effective viscosity computed for the best fitting thermo-mechanical model (see top of Fig. 4).

For comparison, we have chosen two analogue experiments presented in Mattioni *et al.* (2006): a 3D cylindrical experiment (PH1), in which the weak nappe dipping direction is in the direction of stretching (i.e., $\beta = 0^\circ$ in Fig. 4), and a non-cylindrical experiment (PH4), in which the dipping direction is not co-linear with the stretching direction (i.e., $\beta = 30^\circ$ in Fig. 4).

The dip of the weak nappe in the analogue experiments depends on its strike, β, and on its apparent dip in the stretching direction, which is set constant, i.e., $\alpha = 20^\circ$. The two analogue experiments have different scaling because they were run with different velocities of extension. As our final goal is to study the Gulf of Corinth, we have arbitrarily chosen that, at nature scale, the velocity of extension is the same but the viscosities of the viscous layers are different. The rest of the scaling parameters are summarised in Table 2.

Results of the analogue experiments. The results of the experiments PH1 and PH4 are described in the companion paper by Mattioni *et al.* (2006) but are summarized here to allow for comparison. In both experiments, the dipping slab of silicone putty (where it exists) allows for the formation of a rift zone rooted above the silicone, which localizes most of the extension in the elasto-plastic domain. In the early stages of deformation, a system of conjugate high-angle normal faults initiates at the upper tip of the dipping layer and propagates to the free surface as the horizontal offset increases at the level of the dipping slab of silicone. As a result, a roughly symmetrical graben is created. As deformation increases, the first synthetic fault remains fixed with respect to the tip of the silicone slab, whereas the rifted zone slightly propagates in the down-dip direction of the silicone level. This leads to a progressive asymmetrical widening of the basin in which the faults rotate passively to a lower angle. As horizontal strain increases, a large downward flexure progressively deforms the hanging wall of the décollement level but no fault seems to form in this area (see cross-section in Fig. 5).

In the non-cylindrical experiment (PH4), the silicone dipping slab is not present everywhere along the strike. This experiment is thus divided into three structural zones (see Mattioni *et al.* 2006), a first one where the slab is present (left side of the surface view experiment in Fig. 5), a second one where the silicone is not present (right side of the surface view experiment in Fig. 5) and a third one which corresponds to the transition zone.

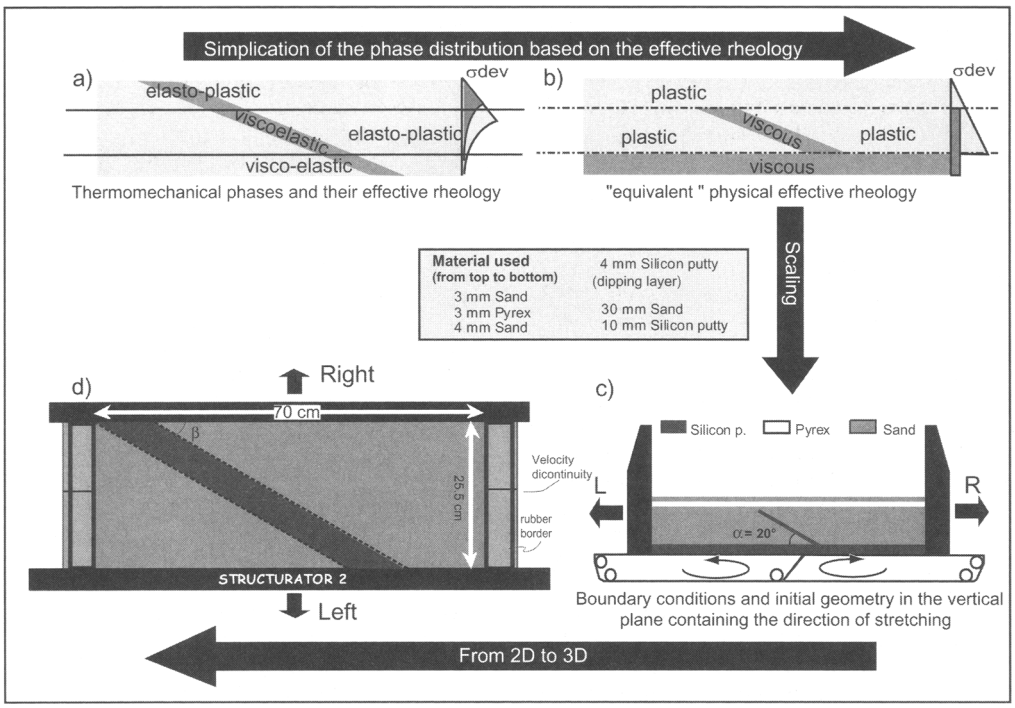

Fig. 4. From thermo-mechanical to analogue modeling: (**a**) Previous thermo-mechanical model and its yield strength envelopes. (**b**) Effective rheology is used to obtain the distribution of viscous and elasto-plastic analogue materials in the analogue experiment. (**c**) Final cross-section of the analogue model in the direction of extension. The apparent dip of the silicone putty in this direction is the same as in the thermo-mechanical model, but the boundary conditions at the base include a velocity discontinuity that is not present in the thermo-mechanical experiment. (**d**) Top view of experiment 4, $\beta = 30°$.

In the first structural zone, the overall trend of the modelled rift is parallel to the strike of the silicone slab. The first fault forming at the tip of the silicone putty maintains its original orientation during the course of the experiments (i.e., parallel to the strike of the underlying viscous layer). The faults forming in the later stage of the experiments are structurally more complex. They nucleate as a system of en echelon faults roughly oriented N105. As the deformation

Table 2. *Scaling parameters for the analogue models PH1 and PH4*

Dimension	Scaling	Nature	Model
L^*	2.5×10^{-6}	4×10^3 m	10^{-2} m
g^*	1	9.8 ms^{-2}	9.8 ms^{-2}
ρ^*	~0.5	2600 kg/m^3	1000–1500 kg/m^3
$V^{*(1)}$	10^4	1 cm/yr	1 cm/hr
$V^{*(4)}$	10^4	1 cm/yr	2 cm/hr
			formula
σ^*	1.25×10^{-6}		$\rho^* \times g^* \times L^*$
$t^{*(1)}$	2.50×10^{-10}		L^*/V^*
$\eta^{*(1)}$	3.13×10^{-16}		$\sigma^* \times T^*$
$T^{*(4)}$	1.25×10^{-10}		L^*/V^*
$\eta^{*(4)}$	1.56×10^{-16}		$\sigma^* \times T^*$

(1) and (4) refer respectively to the analogue experiments PH1 and PH4.

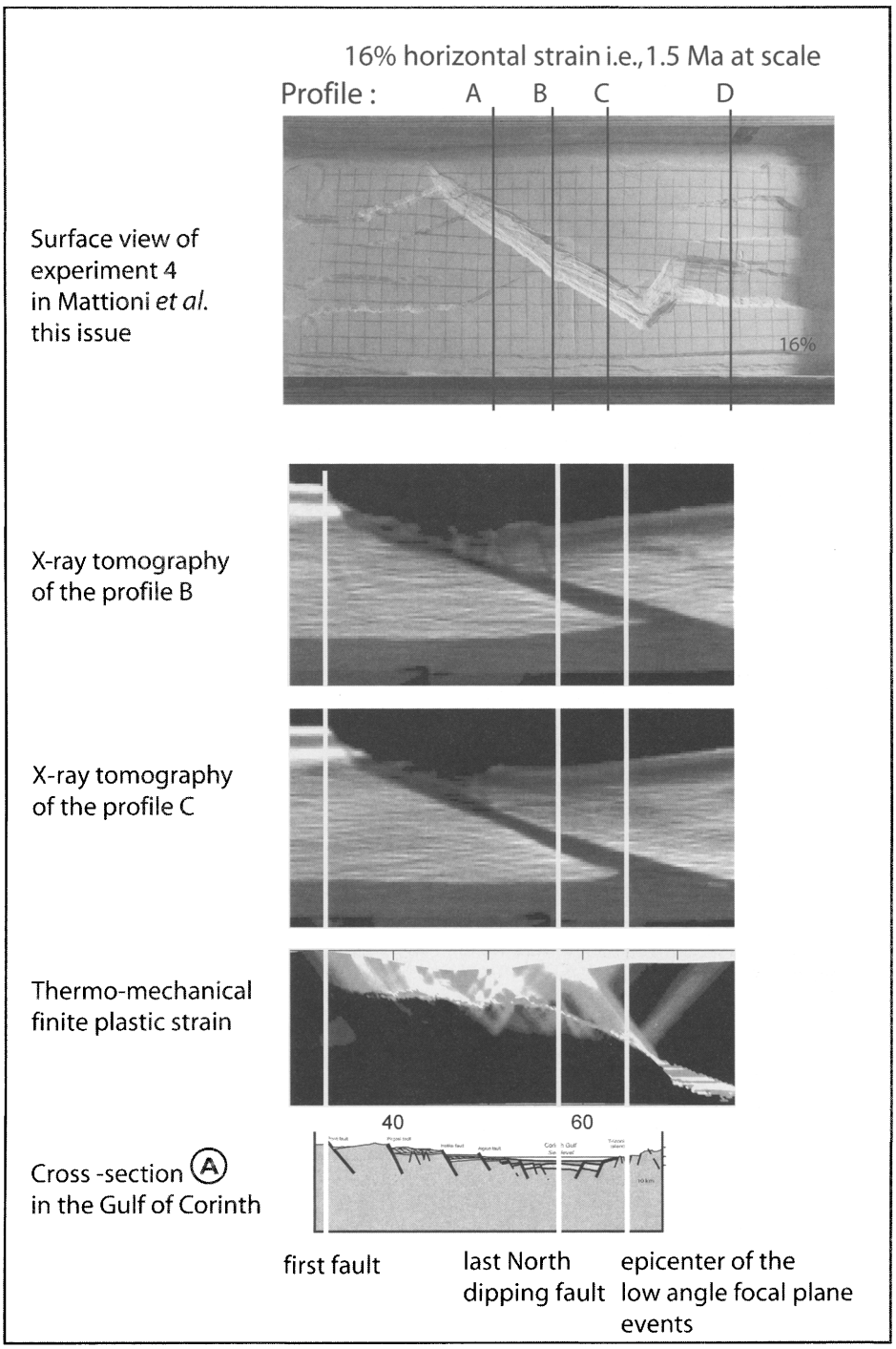

Fig. 5. A comparison between analogue model (PH4), the thermo-mechanical model and a cross-section in the Gulf of Corinth. Top: surface view of experiment PH4 after 16% strain showing the location of the 4 profiles used for comparison. Bottom: All the models are at the same scale, only details of the rifts are displayed. No vertical exaggeration.

progresses, their lateral terminations become progressively parallel to the strike of the viscous layer whereas their central segment remains orthogonal to the direction of extension. This rotation about the vertical axis gives them a roughly sigmoid shape (see surface photography in Fig. 5).

In the second structural zone, rifting is localized in wider grabens striking orthogonal to the direction of extension. Their size reflects the larger thickness of the sand pile. In the third structural zone (i.e., the transition zone), the geometry of the faults depends mostly on the initial geometry of the silicone slab termination (see experiments 2, 3 and 4 in Mattioni *et al.* 2006). However, it is worth noting that in every experiment, the existence of the silicone slab laterally in the model affects the location of the wider grabens in the second structural zone. As soon as the normal faults which border those grabens propagate laterally in the transition zone and further in the first structural zone, their strikes rotate and become perpendicular to the strike of the silicone slab (see surface view in Fig. 5). The strike rotation also occurs for the grabens which nucleate at the rear of the silicone slab (i.e., bottom/left of the surface view in Fig. 5). This rotation does not occur in the cylindrical model and thus cannot be related to border effects. This rotation of the horizontal stress field around the silicone slab suggests that the heterogeneity behaves like an elastic dislocation in the analogue model.

Comparison between thermo-mechanical and analogue experiments (PH 4). Figure 5 shows that the width of the rift as well as the fault spacing obtained in the sandbox experiments is much smaller than in the thermo-mechanical experiment and thus than observed in the Gulf of Corinth. How can those discrepancies be explained?

Some differences are certainly related to the simplifications that had to be done in terms of rheology and boundary conditions for the analogue modelling technique. Rheological assumptions fall into two main groups: (1) the elastic parameters of sand and PDMS are not scaled to the dimension of the model. In other words, elasticity is assumed to be negligible in the problem, and (2) there is no possibility of breaking the silicone putty layer because the transition from brittle to ductile behaviour is abrupt.

Concerning the boundary conditions, two major differences exist between analogue and thermo-mechanical models. Firstly, our 2D numerical models assume plane strain conditions (i.e., no strain occurs in the out-of-plane direction of the numerical model) whereas analogue experiments are 3D. Secondly, bottom boundary conditions differ between the two modelling techniques. The numerical thermo-mechanical models involve isostatic compensation at their base, whereas the analogue models have fixed velocities at their base in both horizontal and vertical direction and display a velocity discontinuity midway between their lateral boundaries where the underlying plastic sheets diverge.

In order to explore the potential effects of contrasting rheology and boundary conditions existing between the two modelling techniques, numerical benchmark tests have been conducted.

Relevance of 2D numerical benchmarks for 3D analogue models

In all the numerical mechanical models, the initial element size is 250×250 m and the thermal coupling is disabled because (1) it is not needed to calculate the viscosity (which is set as constant) and (2) thermal stresses or other Boussinesq terms may only have a little effect on the results but may obscure the comparison with the analogue results.

Setting the numerical benchmarks: the REF and REFSLOW models

In the analogue experiments, silicone behaves as a viscous body and sand as an elasto-plastic body. The same rheological laws are used to compute their numerical benchmarks except that for numerical reasons, the weak silicone slab has been replaced by a Maxwell visco-elastic body with a high shear modulus to ensure that it will always behave as an effectively viscous body. Sand and Pyrex have been replaced by a single elasto-plastic body (see Table 3 for the mechanical constants).

The first aim of the simplified numerical experiments is to reproduce the results of the analogue experiments. The second aim is to use them in order to get a better understanding of the discrepancies existing between the analogue and the thermo-mechanical experiments by varying in the numerical benchmarks the parameters that cannot be varied with the sandbox approach.

In order to simulate analogue experiments, numerical boundary conditions have been set as closely as possible to their analogue counterparts except that the sharp velocity discontinuity at the base has been enlarged to a zone of 10 km in order to limit repeated remeshing which leads to numerical diffusion when computing large strains with a Lagrangian strategy. Paravoz is numerically optimized to enter parameters related to lithospheric processes without previous scaling. Hence, the parameters of the

benchmarks are similar to the parameters of the sandbox but at nature scale. Some parameters are not used to scale the analogue experiments, (e.g., elastic moduli), but are needed for numerical computations. To compute the reference numerical benchmarks, they are set to their most accepted values in nature.

Because the experiments PH1 and PH4 were made with two different stretching velocities and thus two different viscosities at nature scale, two reference benchmarks had to be set up. Their initial and boundary conditions are described in Figure 6. REFSLOW is similar to the 3D cylindrical experiment PH1, while REF is the closest 2D approximation of a cross-section located at profile B in the analogue model PH4.

Results of the numerical benchmarks

REFSLOW and PH1. The first benchmark test compares the 3D cylindrical analogue experiment PH1 with REFSLOW. Figure 7 displays a comparison between their topographic profiles, and highlights that conceivable differences in amplitude and width exist between the numerical experiments and the analogue experiments. Moreover, the first fault is much steeper in the analogue experiment. This analogue modelling artefact is probably due to the presence of a layer of Pyrex, which possesses a higher friction angle than sand and thus leads to a steeper (Coulombs) fault dip angle.

However, the faulting patterns are quite similar. For example, the number of faults present in the main graben as well as their spacing correlate well between the two models. This shows that the resolution used for the numerical benchmark is sufficient to distinguish between plastic shear bands at the same length-scale as those visualized by x-ray tomography.

Testing the relevance of the 2D plane strain assumption for REF and PH4. The first issue concerning the use of a mixed 2D numerical/3D analogue approach is to check the validity of the plane strain assumption through a series of cross-sections. This is important to validate the results of previous thermo-mechanical models as well as the benchmark approach. Four cross-sections oriented in the direction of extension have been chosen in the analogue experiments. Three of them (A to C) cross the weak nappe and the last profile (D) is located in an area where the weak nappe is not present. Their precise location is indicated on a surface picture of experiment PH4 at the top of Figure 5. For 30° of obliquity between the weak nappe and the direction of extension, analogue experiments clearly show two kinds of 3D structures at the surface: en echelon structures at small length scale, and sand-pile-scaled normal faults propagating from the domain where the weak nappe does not exist towards the weak nappe.

Using topography as a control parameter, profiles A, B and C have been compared to three numerical experiments in which the position of the weak nappe varies relative to the border of the model (Fig. 8). The topographic profiles obtained with these 2D plain strain numerical models are different from each other. As in the test with REFSLOW, the numerical experiments slightly underestimate the amplitudes of topography. However, the variation of width of the faulted zone in the numerical benchmarks is consistent with profiles taken in the direction of extension of the analogue model. This suggests that the variation of width of the rift along the strike of the weak nappe in the analogue experiments is not related to out-of-plane propagating structures but to the mean strain rate affecting the hanging wall of the nappe (i.e., where the rift forms). This rate depends on its position relative to the velocity discontinuity and the diverging wall. The results confirm that the weak nappe controls the depth and the location of localization and show that the topography is largely controlled by the dip of the weak nappe in the direction of extension.

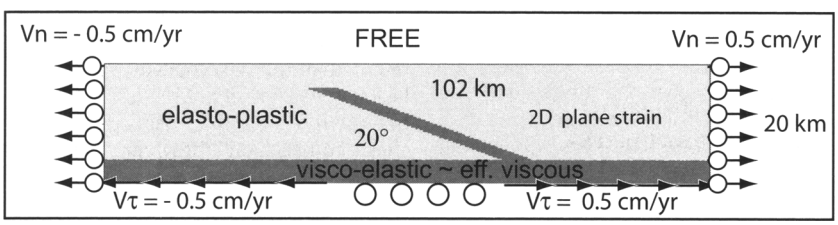

Fig. 6. The distribution of materials in the reference benchmark test, i.e., REF and REFSLOW models, is the same as in the analogue model. The velocity discontinuity at the base has been enlarged to reduce the occurrence of remeshing during computation.

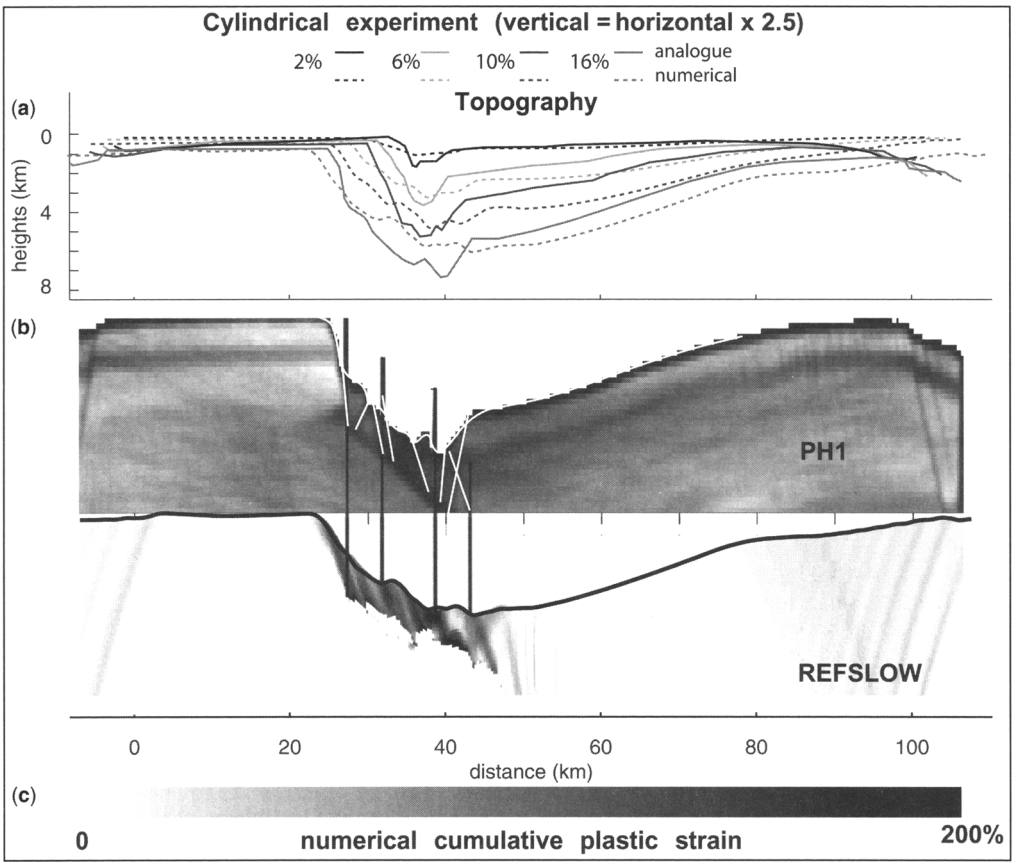

Fig. 7. (**a**): Topographic profiles of the 3D cylindrical experiment PH1 and of the numerical model REFSLOW for different finite stretching. (**b**) Tomographic vertical cross-section of PH1 at 16% stretching with faults and topography interpreted with white lines. (**c**) Cumulative plastic strain at 16% stretching for REFSLOW. The vertical black lines correlate faults between the numerical and the analogue experiments.

A comparison of the x-ray tomographic profile D (at the location where the nappe does not exist) and the cumulative plastic strain in the equivalent numerical model shows that the fault spacing is consistent. However, the location of the grabens differs and suggests that in the analogue model, the location of faults is laterally controlled by the presence of the weak nappe whereas, in the numerical model, it is controlled by boundary effects (Fig. 9).

Testing the effect of rheological assumptions on the benchmarks

Effect of visco-elasto-plasticity in the weak nappe

In the thermo-mechanical experiments, the weak nappe is broken into smaller segments during down dip migration of the subsidence. This phenomenon allows out-of-sequence faults to form at the rear of the major active faults. In the analogue experiments, the weak nappe has a purely viscous behaviour which may prevent the formation of those faults as well as the propagation of faults into the footwall of the weak nappe. To check this possibility, a visco-elasto-plastic (VEP) benchmark test has been computed. By visco-elasto-plastic, we mean that the visco-elastic part of the model has been replaced by a visco-elasto-plastic body with a similar viscosity to that in REF. The comparison between REF and VEP (Fig. 10) shows that a visco-elasto-plastic weak nappe does not affect the width of the faulted zone, but amplifies the effect of the velocity discontinuity by localizing strain rate above it.

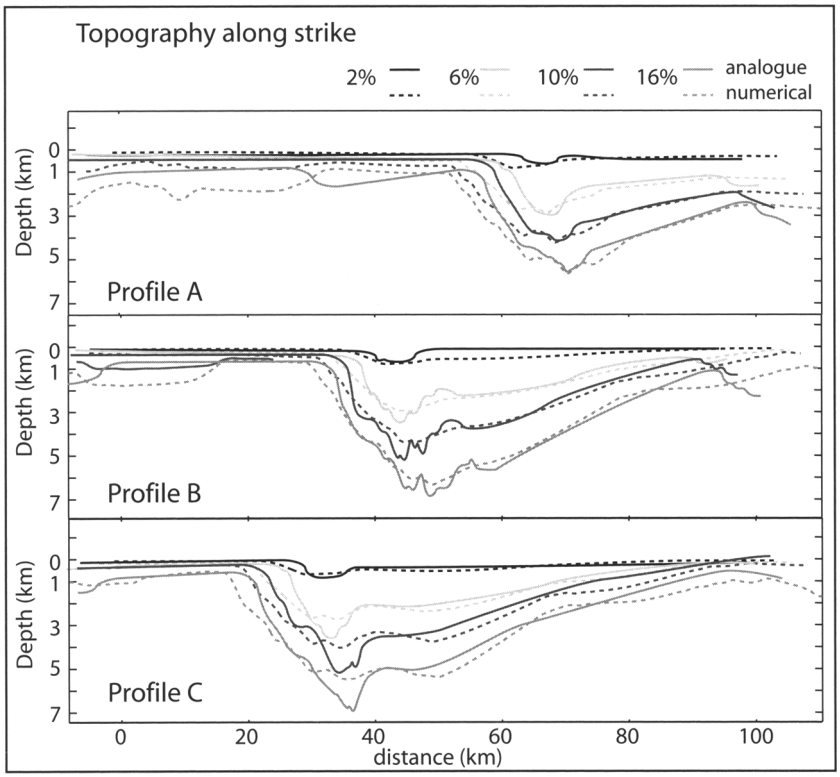

Fig. 8. Analogue model topographies of PH4 experiment are scaled up and shown with dashed lines while their equivalent numerical topographies are represented by plain lines.

Effect of elastic moduli in the elasto-plastic layer

Elastic moduli values are usually not taken into account to scale sandbox experiments. Pa unit parameters are usually scaled following the experimental constrains related to Earth's gravity field, the density of the analogue material, cohesion and dimension of the modelling box.

$$\begin{aligned}\sigma^* &= \rho^* \times L^{*2} \times T^{*-2} \\ &= \rho^* \times L^* \times g^*\end{aligned} \tag{8}$$

where σ^*, ρ^*, g^* and T^* stand respectively for non-dimensional values of stress, density, gravitational acceleration ($g^* = 1$) and time.

Taking an accepted value of 10^7 Pa (e.g., Vermeer 1990) for the shear modulus of sand and the scaling parameters of experiment 4, the shear modulus G at Earth scale becomes:

$$\begin{aligned}G^{\text{at scale}} &= \frac{G^{\text{sand}}}{\sigma^*} \\ A.N.{:}G^{\text{at scale}} &= 8 \times 10^{12}\ \text{Pa}\end{aligned} \tag{9}$$

This value is far higher than values obtained from the PREM model (Poirier 2000) where the highest value is 2.9×10^{11} Pa at the core mantle boundary. Moreover, it differs by two orders of magnitude from the values obtained

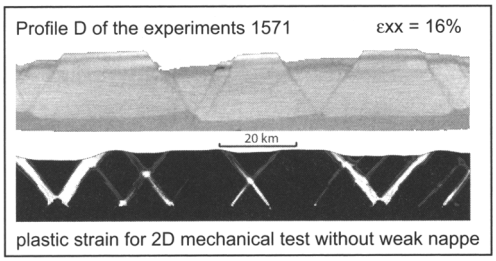

Fig. 9. Cumulative plastic strain without the weak nappe (bottom) is compared with profile D of exp. PH4 (top). In the numerical results, white stripes correspond to localized plastic strain.

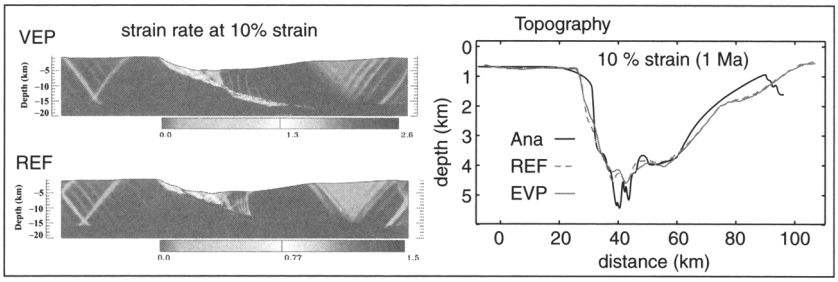

Fig. 10. The effect of a visco-elastic-plastic rheology for the weak nappe. VEP: visco-elasto-plastic; REF: reference model; ANA: experiment PH4 profile B.

for the crust, e.g., 2×10^{10} Pa (Turcotte & Schubert 2002).

However, mechanical codes based on continuum mechanics (e.g., Paravoz) account for an elasto-plastic rheology, and the elastic moduli need to be set. In the REF experiments, elastic moduli are set to values that are relevant for rocks. To test the effects of mis-scaling elastic moduli, we vary their values by one order of magnitude above and below the commonly accepted value for Earth. The resulting topographies for different finite strains are plotted in Figure 11. They suggest that increasing elastic moduli values in the elasto-plastic layer leads to an increase of the topographic amplitudes for a given finite strain.

The misfit between REF and $\times 0.1$ experiments is bigger than between REF and $\times 10$ experiments because the faults (see cumulative plastic strain on Fig. 11) do not propagate down to the basal viscous layer in the model ($\times 0.1$). However, numerical results obtained with an over-estimated elastic coefficient fit much better with the topography of analogue experiments. This means that one should properly scale the elastic properties of sand by adjusting the density or the dimension of the box as much as possible. However, it is very difficult to determine the elastic properties of granular media like sand as they are very sensitive to damage and strain-rate (e.g., Lyakhovsky *et al.* 1993). This misfit highlights a more general problem: is the sand a good analogue for crust? How far do sand and silicone interact elastically? It is beyond the scope of this study to answer those questions because the set-up, dedicated to the Gulf of Corinth, is too complicated to get quantitative insights into these problems and this kind of study should be done by carefully checking the elastic properties of the sand used for the experiments, especially its Poisson coefficient. However, it seems that benchmarks with numerical codes may be helpful in solving this problem.

Testing boundary conditions

Type of boundary conditions

Boundary conditions in the analogue experiments are characterized by a horizontal velocity discontinuity where the underlying sheets diverge and by a vertical velocity set to zero at the base of the models. This differs significantly from the isostatic conditions that were imposed in the thermo-mechanical experiments and leads to the observation that the footwall of the weak nappe hardly rotates in the analogue experiments.

In order to explore the effects of a larger range of boundary conditions, several benchmarks have been run. One of them reproduces the exact boundary conditions of the coupled thermo-mechanical computations (i.e., B4 in Fig. 12) but, as this kind of basement is not available in the analogue experimental device, intermediate boundary conditions available in the lab have been tested. One way to simulate local isostasy is to use a thicker layer of silicone putty at the base of the model. As it is not possible to increase the vertical size of the analogue model, the thickness of the basal layer has been multiplied only by a factor 2. The effect of the basal velocity discontinuity on the results has also been investigated by changing it into free slip boundary conditions in the numerical model.

Results

The strain rates resulting from a wide range of boundary conditions after 10% of bulk extension (Fig. 12) show that the velocity discontinuities, at the base and at the level of the weak nappe, interact to form some parasitic synthetic (almost vertical) faulting at the front of the basin. Such faults are sometimes observed in the analogue results.

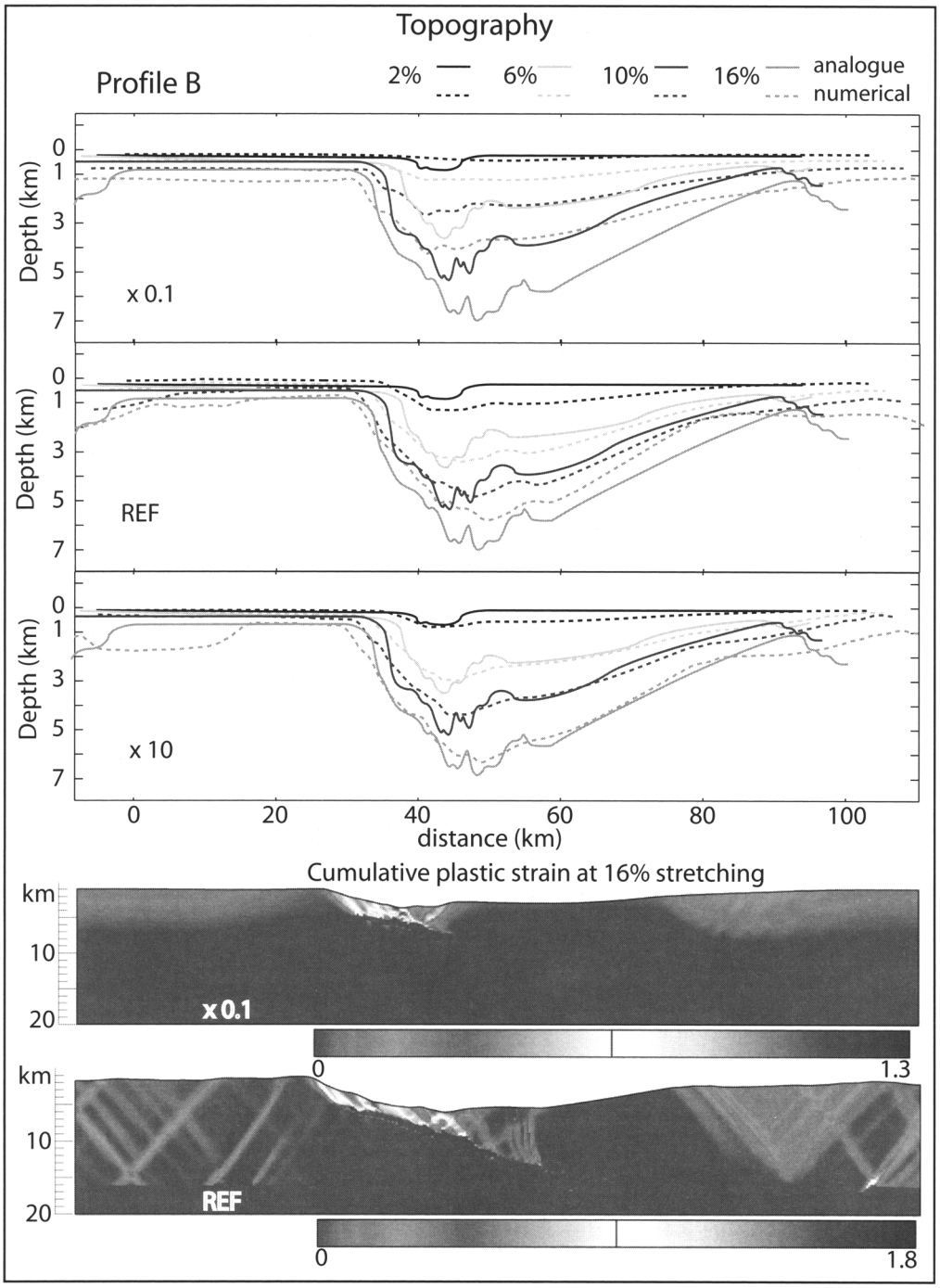

Fig. 11. The effect of misscaling of the elastic parameters. Dashed lines show topography at the level of profile B in analogue experiment PH4. Drawn lines represent the topography computed for three different value of shear modulus (Poisson coefficient kept constant at 0.25). A better fit is obtained for over-estimation of the shear modulus.

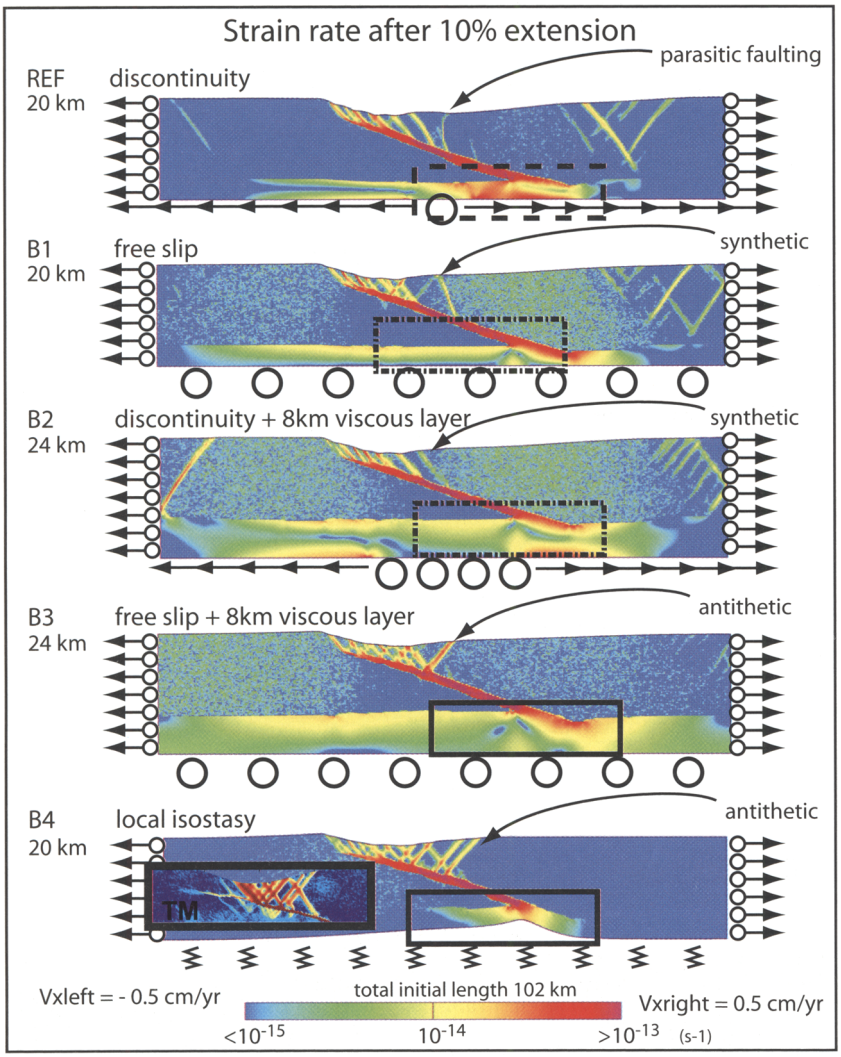

Fig. 12. Strain rate after 10% of bulk extension for a range of boundary conditions at the base: REF: Boundary conditions include a sharp velocity discontinuity in the centre. The base of the model is made of 4 km of viscous body (i.e., 1 cm of silicone putty). B1: Same geometry and vertical velocity to REF model but the base of the model is a free slip surface. B2: Same boundary conditions to REF but 4 km (equivalent to 1 cm of silicone putty) has been added at the base. B3: Same geometry to B2 with the boundary condition of B1. B4: Winkler basement equivalent to the boundary condition of the thermo-mechanical model in Le Pourhiet *et al.* (2004).

For comparison, we also add at the edge of the isostatic case in Figure 12, a detail of strain rate in the thermo-mechanical model for the same amount of bulk extension. It outlines that antithetic faults are active during the formation of the graben. These faults are only present in the B3 and B4 models. These models have their basal boundary conditions closest to those of the thermo-mechanical experiments. However, this detail of the thermo-mechanical results also shows discrepancies with the benchmarks. There are much less active faults in this more realistic experiment. This inactivity of the oldest fault is caused by the presence of faults crossing the footwall which annihilate the shear on the weak nappe and thus relate to the discussed rheological simplifications.

Table 3. *Mechanical properties of the mechanical benchmark test materials*

Properties mat.	Density (kg/m^3)	Shear modulus (Pa)	Poisson ratio	Viscosity (Pa s)	Friction angle	Dilatation angle
Elasto-plastic	2700	3×10^{10}	0.25	no	34°	0°
Visco-elastic		3×10^{11}	0.25	1.25×10^{20}	no	no

Comparing REF and B2 with the other experiments suggests that the removal of the discontinuity at the base permits the antithetic faults to form. However, increasing the thickness of the basal silicone layer is a major factor in widening the rift, because it is the only one that permits the weak layer to flatten by rotation of the footwall (exp. B4). This phenomenon was shown by Le Pourhiet *et al.* (2004) to be one of the effective mechanisms for migration of the basin in the thermo-mechanical models, because upward flexure of the footwall favours faulting (Buck 1988). The annihilation of this flexure in the analogue experiments causes (1) all the faults to remain active, (2) the suppression of the synthetic out-of-sequence faults growth, and (3) the formation of a single basin instead of multiple half-grabens. All dynamic features observed in the thermo-mechanical model thus disappear in favour of a fully kinematically constrained model.

Conclusion on the methodology

Our benchmark tests have shown that for our set-up: (1) The fact that the elastic coefficients are not correctly scaled with nature in the analogue experiments affects the models. However, in this special setting, the boundary conditions at the base and the weak nappe completely control the kinematics and it is difficult to evaluate quantitatively the effect of this mis-scaling. (2) The 2D plane strain approximation used in the thermo-mechanical experiments is valid as long as the weak nappe is present.

Analogue models give insights into expected fault patterns for a real 3D setting which, for software and hardware reasons, cannot be modelled with current numerical tools, but are very limited in terms of available boundary conditions, scaling, and/or acquisition of the results. The sharp rheological contrasts inside the model, as well as the scaling limitation, cause some parasitic phenomena which can easily be isolated using numerical benchmarks of the analogue models. In the present study these benchmark tests have shown that:

(1) The velocity discontinuity at the base of the models interferes with the discontinuity created by the rheological contrast of the weak nappe and leads to the formation of parasitic faults responsible for artefact topographic heights observed in both numerical and analogue models (profile B in Fig. 8).
(2) The vertical dimension of the modelling box, which is constrained by the size of the medical scanner used for the acquisition, does not allow us to put a thick viscous layer at the base of the experiments. The boundary conditions at the base lead to the annihilation of the formation of some of the principal structural features, i.e., faulting in the footwall and migration of the basin by flexural flattening of the weak nappe.

Thus, mixed methodology is a very useful tool because it leads to a better understanding of the features observed in the analogue models. This approach also helps to save time and money for 3D case studies because it enables some analogue experiments to be skipped.

Is the 3D model valid for the Gulf of Corinth?

The 3D analogue and 2D numerical experiments have outlined that:

(1) The results of our previous thermo-mechanical study are only valid if local isostatic compensation occurs at the scale of the upper crust; i.e., the thickness of the elasto-plastic layer should be rather small compared to the thickness of the effectively viscous lower crust. In the case of the Gulf of Corinth, this hypothesis is acceptable, because the elasto-plastic layer extends down to the brittle ductile-transition, i.e., approximately 10–12 km (Rietbrock *et al.* 1996; Rigo *et al.* 1996; Pham *et al.* 2000; Lyon Caen *et al.* 2004), and because the crust is thick enough (40–45 km, according to Makris (1978) and Tiberi *et al.* (2001) to allow for the lower crust to diffuse in short times any displacements at small length scales (5–10 km).
(2) The en echelon structure and the lack of field evidence for major transverse faults can be explained by the discrepancy between the current direction of extension and the dipping direction of the weak heterogeneity.

(3) The seismic events relocated on SW/NE trending faults may not take place on inherited faults as suggested by Lyon Caen *et al.* (2004) but rather on newly-formed transverse normal faults.
(4) The comparison between analogue models and their mechanical numerical benchmarks suggest that the presence of a weak heterogeneity acts as a localizing factor even laterally where the Phyllades nappe does not exist, e.g., in the internal zone of the Hellenides corresponding to the eastern part of the rift.

However, these 3D analogue models and their mechanical benchmarks were not able to reproduce the kinematics (in and out-of-sequence faulting) and the geometry (multiple half-grabens) of the faults in the western part of the Gulf which is obtained with the 2D thermo-mechanical models.

Neither of the two modelling techniques taken separately would have been able to propose an explanation for the 3D dynamics of faulting in the Gulf of Corinth because (1) the boundary conditions imposed by technical limitations of the analogue method do not give full access to the dynamics of the problem, and (2) 3D numerical methods are not efficient enough yet (memory and CPU) to get insights into 3D mechanically consistent shear banding with large strains.

Our study has shown that, by using a mixed approached with a large set of geological data, it is possible to overcome these limitations. The results obtained by this type of approach are, however, case sensitive, because data are needed to test the models at each stage before making new assumptions or approximations. In our study, the dip and the burial depth to the sheet of silicone putty did not change during the analogue experimentation. These two parameters were deduced from systematic numerical modelling results to reduce the number of analogue experiments.

Thanks to E. Burov for helpful discussion and free use of his version of Paravoz (a Podladchickov & Poliakov[ltd] code). J. P. Brun and J. Smit are thanked for their useful comments during the meeting as well as S. Buiter, O. Dauteuil, C. Pascal and an anonymous reviewer for their careful, time-consuming but very useful reviews.

References

ARMIJO, R., MEYER, B. *ET AL.* 1996. Quaternary evolution of the Corinth rift and its implications for the late Cenozoic evolution of the Aegean. *Geophysical Journal International*, **126**, 11–53.

AUBOUIN, J., BONNEAU, M. *ET AL.* 1970. Contribution à la géologie des Hellènides: le Gavrovo, le Pinde et la zone ophiolitique subpélagonienne. *Annales Société Geologique du Nord*, **90**, 277–306.

BENTHAM P., COLLIER, R. E. L. *ET AL.* 1991. Tectono-sedimentary development of an extensional basin: the Neogene Megara Basin, Greece. *Journal of the Geological Society*, **148**, 923–934.

BOS, B. & SPIERS, (2002). Frictional-viscous flow of phyllosilicate-bearing fault rock: Microphysical model and implications for crustal strength profiles. *Journal of Geophysical Research*, **107**, 2028, DOI: 10.1029/2001JB000301.

BRIOLE, P., RIGO, A. *ET AL.* 1999. Active deformation, of the Gulf of Korinthos, Greece: results from repeated GPS surveys between 1990 and 1995. *Journal of Geophysical Research*, **105**, 25605–25625.

BUCK, W. R. 1988: Flexural rotation of normal faults. *Tectonics*, **7**, 959–993.

CHEN, Y. & MORGAN, J. 1990. A non-linear rheology model for mid-ocean ridge axis topography. *Journal of Geophysical Research*, **95**, 17583–17604.

CAUSSE, C., MORETTI, I. *ET AL.* 2004. Kinematics of the Corinth Gulf inferred from calcite dating and syntectonic sedimentary characteristics. *Comptes Rendus Geoscience*, **336**, 281–290.

COCARD, M., KHALE, H. *ET AL.* 1999. New Constraints on the rapid motion of the Aegean region: recent results inferred from GPS measurements (1993) across the West Hellenic Arc, Greece. *Earth and Planetary Science Letters*, **172**, 39–47.

COLLETTA B., BALÉ, P. *ET AL.* 1991. Computerized x-ray tomography analysis of sandbox models: examples of thin-skinned thrust systems. *Geology*, **19**, 1063–1067.

CUNDALL, P. A. 1989. Numerical experiments on localization in frictional materials. *Ingenieur Archiv*, **59**, 148–159.

CUNDALL, P. A. & BOARD, M. 1988. A microcomputer program for modelling large-strain plasticity problems. *In*: SWOBODA, C. (ed.) *Numerical Methods in Geomechanics*, Balkema, Brookfield, 2101–2108.

DUERMEIJER, C. E., NYST, M. *ET AL.* 2000. Neogene evolution of the Aegean arc: palaeomagnetic and geodetic evidence for a rapid and young rotation phase. *Earth and Planetary Science Letters*, **176**, 509–525.

DOUTSOS, T. & KOKKALAS, S. 2001. Stress and deformation patterns in the Aegean region. *Journal of Structural Geology*, **23**, 455–472.

FLOTTÉ, N. 2002. Caractérisation structurale et cinématique d'un rift sur détachement: le rift de Corinthe-Patras, Grèce. PhD thesis, Université Paris Sud.

GHISETTI, F. & VEZZANI, L. 2004. Plio–Pleistocene sedimentation and fault segmentation in the Gulf of Corinth (Greece) controlled by inherited structural fabric. *Comptes Rendus Geoscience*, **336**, 243–249.

GHISETTI, F., VEZZANI, L. *ET AL.* 2001. Tectonic setting and sedimentary evolution of the southwest margin of the Corinth rift (Aigion-Xylocastro area). Public vol. 56207.

JACKSON, J. A., GAGNEPAIN, J. *ET AL.* 1982. Seismicity, normal faulting and the geomorphological development of the Gulf of Corinth (Greece): the Corinth earthquakes of February and March 1981. *Earth and Planetary Science Letters*, **57**, 377–397.

JOLIVET, L. & FACCENNA, C. 1999. The kinematics of back arc basins, examples from Tyrrhenian, Aegean and Japan seas. *In*: MACNIOCAILL, C. & RAYAN, P. D. (eds), *Continental Tectonics*, Geologial Society, London, Special Publications, 21–53.

JOLIVET, L., BRUN, J. P. *ET AL.* 1994. 3D kinematics of extension in the Aegean region from the early Miocene to the present, insights from the ductile crust. *Buletin Société Geologique France*, **165**, 195–209.

LATORRE, D., VIRIEUX, J. *ET AL.* (2004). Converted seismic wave investigation in the Gulf of Corinth from local earthquakes. *Comptes Rendus Geoscience*, **336**(4–5), 259–267.

LE POURHIET, L. 2004. Modélisation thermomécanique de l'extension continentale: developpement theorique et applications au golfe de Corinthe (Grèce), Laboratoire de Tectonique, UPMC, 241.

LE POURHIET, L., BUROV, E. B. *ET AL.* 2004. Rifting through a stack of inhomogeneous thrusts (study case in the Gulf of Corinth). *Tectonics*, **23**, TC4005.

LYKOUSIS, V., SAKELLARIOU, D. *ET AL.* 1998. Sequence stratigraphy in the N. margin of the Gulf of Corinth: implication to upper Quaternary basin evolution. *Bulletin of the Geological Society of Greece*, **XXX**, 157–164.

LYON CAEN, H., PAPADIMITRIOU, P. *ET AL.* 2004. On the seismicity of the Corinth Rift laboratory area. *Comptes Rendus Geoscience*, **336**.

LYAKHOVSKY, V., PODLADCHIKOV, Y. *ET AL.* (1993). A rheological model of a fractured solid. *Tectonophysics*, **226**, 187–198.

MAKRIS, J. 1978. the crust and upper mantle of the Aegean from deep seismic soundings. *Tectonophysics*, **46**, 269–284.

MALARTRE, F., FORD, M. *ET AL.* 2004. Preliminary biostratigraphy and 3D geometry of the Vouraikos Gilbert-type fan delta, Gulf of Corinth, Greece. *Comptes Rendus Geoscience*, **336**, 269–280.

MATTIONI, L., LE POURHIET, L. *ET AL.* 2006. Fault pattern produced by extension through a heterogeneous crust: new insights from analogue models. *In*: BRUITER, S. J. H. & SCHREURS, G. (eds), *Analogue and Numerical Modelling of Crustal Processes*. Geological Society, London, Special Publications.

MICARELLI, L., MORETTI, I. *ET AL.* 2003. Influence of depth and amount of displacement of the characteristics of normal faults, case study in the Gulf of Corinth–Greece. *Journal of Geodynamics*, **36**, 275–303.

MORETTI, I. 2004. Asymetry of the early rift structures: a comparison between the Gulf of Suez and the Gulf of Corinth. *In: COST-ACTION 625: Actives Faults: Analysis, Processes and Monitoring*, Camerino, Italy, EDIMOND, 105–111.

MORETTI, I., SAKELLARIOU, D. *ET AL.* 2003. The Gulf of Corinth: a half graben? *Journal of Geodynamics*, **36**, 323–340.

MRLINA, J. 2004*a*. Complex gravimetric investigation of active faults around Aigion, Gulf of Corinth, Greece. *Extended Abstracts, 66th EAGE Conference and Exhibition*, Paris.

MRLINA, J. 2004*b*. Structures and tectonics derived from gravity survey around Aigion, Gulf of Corinth, Greece. *Proceedings 5th International Symposium on Eastern Mediterranean Geology*, Thessaloniki, Greece, **1**, 138–140.

NAVILLE, C., SERBUTOVIEZ, S. *ET AL.* 2004. Pre-drill surface seismic in the vicinity of the AIG-10 well and post-drill VSP. *Comptes Rendus Geoscience* **336**(4–5), 407–414.

PHAM, V. N., BERNARD, P. *ET AL.* 2000. Electrical conductivity and crustal structure beneath the central Hellenides around the Gulf of Corinth (Greece) and their relationship with the seismotectonics. *Geophysical Journal International*, **142**, 948.

POIRIER, J. P. 2000. *Introduction to the Physics of the Earth's interior*. 2nd edn, Cambridge University Press.

POLIAKOV, A. N. B., PODLADCHIKOV, Y. Y. *ET AL.* 1993. Initiation of salt diapirs with frictional overburden: Numerical experiments. *Tectonophysics*, **228**, 199–210.

RAMBERG, H. 1981. *Gravity, Deformation and the Earth's Crust*. Academic Press, New York.

RANALLI, G. 1987. *Rheology of the Earth: Deformation and Flow Processes in Geophysics and Geodynamics*, Allen and Unwin, Boston.

RIETBROCK, A., TIBERI, C. *ET AL.* 1996. Seismic slip on a low angle normal fault in the Gulf of Corinth: evidence from high resolution cluster analysis of microearthquakes. *Geophysical Research Letters*, **14**, 1817–1820.

RIGO, A., LYON-CAEN, H. *ET AL.* 1996. A microseismic study in the western part of the Gulf of Corinth (Greece) implications for large-scale normal faulting mechanisms. *Geophysical Journal International*, **126**, 663–688.

STEFATOS, A., PAPATHEODOROU, G. *ET AL.* 2002. Seismic reflection imaging of active offshore faults in the Gulf of Corinth; their seismotectonic significance. *Basin Research*, **14**, 487–502.

TIBERI, C., DIAMENT, M. *ET AL.* 2001. Moho topography beneath the Corinth Rift area (Greece) from inversion of gravity data. *Geophysical Journal International*, **145**, 797–808.

TROTET, F. 2000. Exhumation des roches de haute pression- basse temperature le long d'un transect des Cyclades au Péloponnèse (Grèce). Implications géodynamiques. PhD thesis?, Université Paris XI.

TURCOTTE, D. L. & SCHUBERT, G. 2002. *Geodynamics*; 2nd edn, Cambridge University Press.

VERMEER, P. A. 1990. The orientation of shear bands in biaxial tests. *Geotechnique*, **40**, 223–236.

VERMEER, P. A. & DE BORST, R. (1984). Non-associated plasticity for soil, concrete and rock. *HERON*, **29**(3), 1–64.

WEIJERMARS, R. 1986. Flow behaviour and physical chemistry of bouncing putties and related polymers in view of tectonic laboratory applications. *Tectonophysics*, **124**, 325–358.